TURBOMACHINERY & PUMP SYMPOSIA | HOUSTON, TX
SEPTEMBER 13-15, 2022
SHORT COURSES: SEPTEMBER 12, 2022

PREDICTING AND CORRECTING NONLINEAR VIBRATION GROWTH IN TILTING PAD JOURNAL BEARINGS UNDERGOING LARGE-AMPLITUDE WHIRL

Richard Armentrout
Fellow Engineer
Curtiss-Wright, Electro-Mechanical Division
Cheswick, Pennsylvania, USA

Richard Armentrout is a Fellow Engineer at Curtiss-Wright in Cheswick Pennsylvania, where he leads fluid film bearing and rotordynamics technology programs in support of various commercial and DOD development efforts on products ranging from subsea electric submersible pumps to water-lubricated canned-motor coolant pumps used in nuclear power plants. Prior to joining Curtiss-Wright, Dr. Armentrout worked for various bearing companies including KMC division of Cookson America and CentriMarc Division of IMO Industries, where he designed fluid film bearings and conducted rotordynamic studies on a wide variety of turbomachinery. Dr. Armentrout also worked in structural dynamics and vibration isolation at McDonnell Douglas, Lockheed-Martin, and Westinghouse. Dr. Armentrout received his B.S.M.E. (1978) and M.S.M.E. (1983) degrees from the University of Virginia, and his Ph.D. (1998) degree from Vanderbilt University. He is a registered professional engineer in the state of Tennessee.

ABSTRACT

When machines equipped with tilting pad bearings are well enough balanced to limit the journal whirl amplitudes to less than 40% to 50% of the bearing clearance, the bearing behavior can usually be considered linear and the pad pivots usually stay loaded radially against the bearing housing without pivot separation. However, if unbalance or other excitations impose higher journal whirl amplitudes that exceed 50% of the bearing clearance, pivot separation or "rattle" can occur between the pad pivots and the supporting bearing housing, leading to increased clearances and vibration. Along with pivot separation, nonlinear bearing stiffening under increasing whirl amplitudes can elevate the critical speed in parallel with the running speed, leading to violent motions at a point of response instability often referred to as a "nonlinear jump". A 35-year-old case study of a single-stage overhung compressor is revisited to investigate whether the above phenomena played a role in compromising the original machine's longevity. The compressor experienced a high unbalance condition due to abrasive erosion of the impeller. The resulting increase in journal motion lead to rapid pivot wear within the original rocker-pivot tilting pad bearings, causing repeated unplanned shutdowns. Basic linear analyses conducted 35 years ago provided bearing and shaft upgrades that were sufficient to restore the machine's reliability at the time. However, a new rotordynamic model having the ability to represent tilting pad bearing nonlinearity has deepened the understanding beyond that of the original linear study. After a summary of its theoretical basis, the new model is exercised to illustrate the potential for nonlinear bearing behavior in the original machine, and subsequently to demonstrate the benefits of additional bearing modifications in mitigating the nonlinear behavior even more effectively than the original shaft modifications performed 35 years ago.

INTRODUCTION

The tilting-pad radial bearing is by far the most universally-prescribed design for machines that can become susceptible to rotordynamic instability. The superior rotordynamic stability comes from the reduction of cross-coupled stiffness that occurs when pads are free to tilt about their individual pivot points. This interrupts the destabilizing tangential oil film forces that can induce catastrophic sub-synchronous vibration in machines equipped with conventional fixed-geometry bearings. Applications range from small high-speed machines such as turbochargers and compressors, to very large equipment such as steam turbines and generators.

A number of authors (1-13) have tested and analyzed tilting-pad radial bearings and compared their performance characteristics to those of conventional fixed-geometry bearings. He, Branagan, and Earles (14-16) have conducted extensive studies into the effects of pad mechanical and thermal deformations on the hydrodynamic performance of tilting-pad bearings. Their efforts have led to sophisticated

thermoelastohydrodynamic (TEHD) computer programs that model the mechanical, thermal, and hydrodynamic attributes simultaneously. These programs calculate the hydrodynamic pressures iteratively in conjunction with the pad tilt angles and journal position to find a state of static load equilibrium. The film pressures and thermal distributions are applied to the pad structural models to compute the film shape changes from mechanical and thermal distortions. Program output typically includes film thickness, temperatures, dynamic coefficients, and power loss.

While the above TEHD solutions offer valuable assessments of performance for most bearing applications, they are limited by the assumption of linearity inherent to steady-state solutions. A steady-state solution solves the hydrodynamic and thermal formulations for a journal equilibrium position based on the loads and speeds, and then calculates the linearized stiffness and damping values for use in estimating the forces due to small journal motions. If, however, unbalance loads or other shaft excitations cause journal motions to exceed around 50% of the clearance as illustrated in Figure 1, the behavior can enter a nonlinear regime where the orbit becomes non-circular and the linearized stiffness and damping are no longer sufficient. In this case, the orbit amplitude reaches about 68% of the bearing clearance and all four pivots undergo momentary separation from the bearing housing. The results in Figure 1 were generated using a nonlinear bearing model (discussed later) having the ability to represent the instantaneous journal and pad motions in response to nonlinear forces within the bearing films and pad pivots

The following discussion begins with a description of the mechanics of pivot separation including the forces acting at each stage of the journal orbit. This is followed by a review of a new nonlinear tilting pad bearing model developed to capture the onset of pivot separation and nonlinear phenomena. The model is then applied to refresh a case study of a problematic single-stage compressor that was preformed 35 years ago using linear analysis tools. The new results confirm the original diagnosis and design remedies, showing very high pivot loads and impacting when journal amplitudes increase under high unbalance. Finally, the new model is used to develop an alternate bearing design that would be more effective in reducing pivot unloading and wear than the simple shaft modifications invoked 35 years ago.

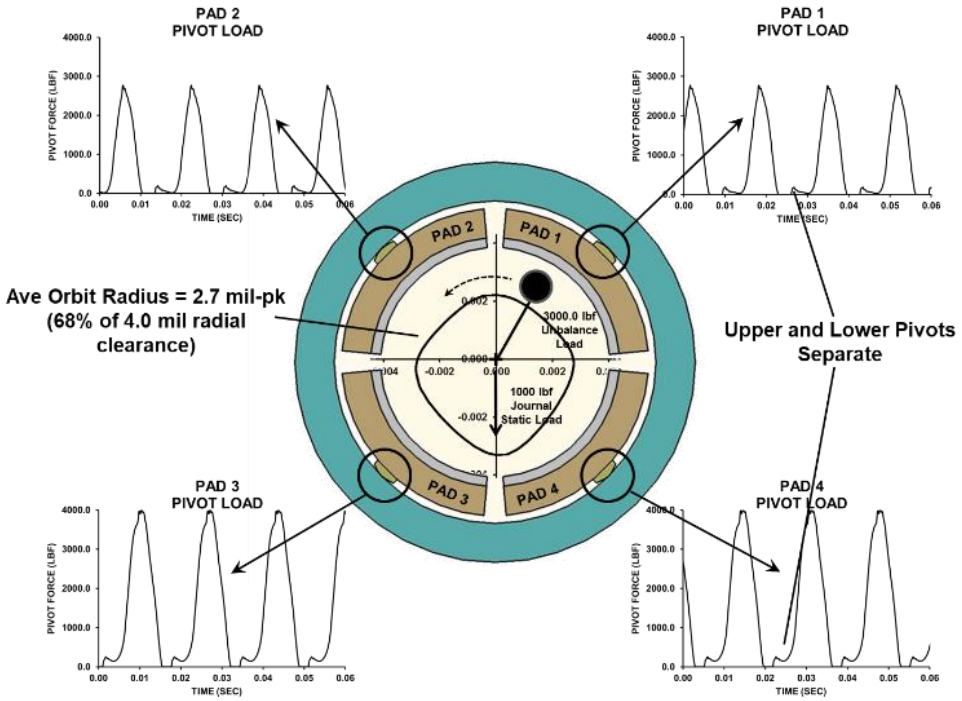

Figure 1. High-Amplitude Journal Whirl Orbit with Pivot Unloading Under Static and Dynamic Journal Loading

MECHANICS OF PIVOT SEPARATION

Plotted in Figures 2 through 4 are calculated shaft whirl motions and the associated film/pivot loads for three levels of increasing journal whirl amplitude in an example 4-pad bearing whose attributes are listed in Table 1. The calculations were performed using a nonlinear tilting pad bearing model (described later) capable of predicting pivot separation.

Table 1
Example Bearing Geometry and Operating Parameters

Bearing Type	Tilting Pad
No. of Pads	4
Axial Length	4.0 in
Diameter	5.0 in
Pad Arc Length	75.0 deg
Radial Set Clearance	0.004 in
Preload	0.2
Pivot Offset	0.5
Oil Viscosity	3.0×10^{-6} lbf-sec/in^2
Speed	3600 RPM
Static Load	1000.0 lbf (downward)

In Figure 2, where the rotating unbalance was set to a low magnitude of 1000.0 lbf, it is evident that the orbit remains nearly circular and within about 35% of the bearing radial clearance. The orbit is offset slightly downward due to a 1000.0 lbf downward static load. Since the whirl amplitude is low, the pivot load oscillations are small and all four pivots remain in contact with the bearing housing (positively loaded).

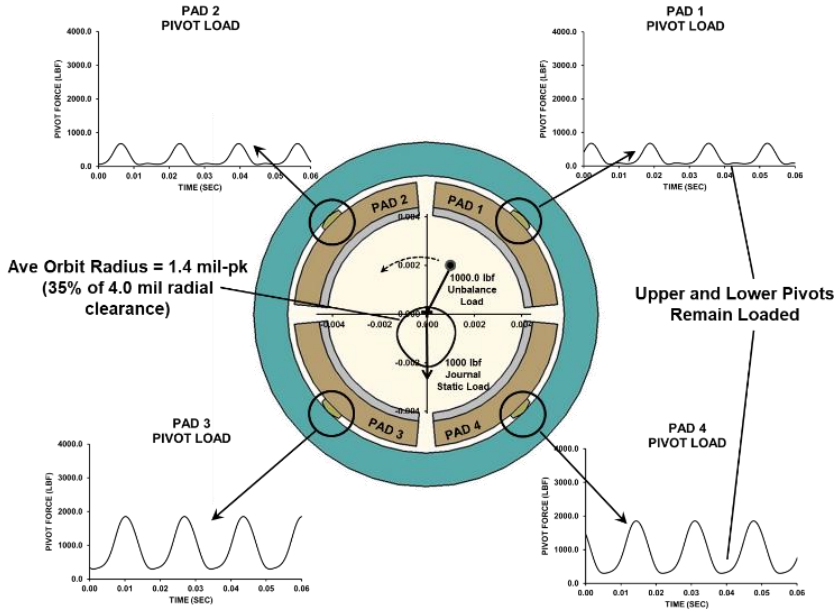

Figure 2. Nonlinear Journal Whirl Orbit and Dynamic Pivot Loads with 1000.0 lbf Rotating Unbalance Load

When the unbalance force is doubled from 1000.0 lbf to 2000.0 lbf, the orbit increases to about 52% of the bearing clearance as shown in Figure 3. The upper pivots now separate, as evidenced by the intermittent periods of zero pivot load. The orbit also has the beginnings

of a four-lobed shape, reflecting the nonlinear stiffness variations as the journal traverses from on-pad ("stiff") positions to between-pad ("soft") positions around the orbit. Pivot separation results from the negative damping forces in the hydrodynamic film that temporarily "pull" the pads away from the housing.

Further increasing the unbalance force to 3000.0 lbf increases the orbit amplitude to about 68% of the bearing clearance as shown in Figure 4. The orbit now has a distinct four-lobed shape driven by the highly-nonlinear film forces at the high orbit amplitude. All four pad loads now reflect momentary pivot unloading that is accompanied by a bounce, or "rattle" spike each time a pivot closes against the housing. If such pivot separation and impacting is allowed to continue, pivot wear and fretting can lead to increased bearing clearances, higher vibration, and unplanned outages.

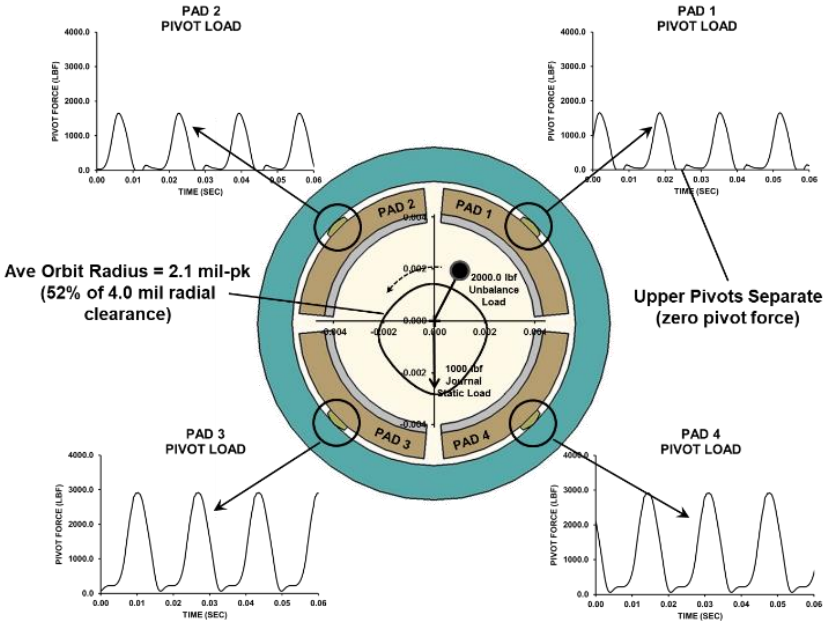

Figure 3. Nonlinear Journal Whirl Orbit and Dynamic Pivot Loads with 2000.0 lbf Rotating Unbalance Load

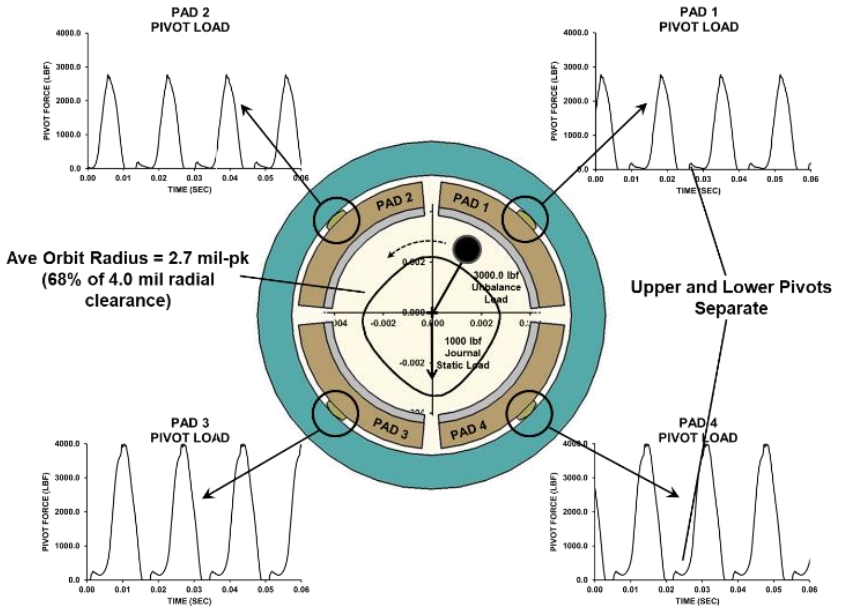

Figure 4. Nonlinear Journal Whirl Orbit and Dynamic Pivot Loads with 3000.0 lbf Rotating Unbalance Load

Further understanding of the forces governing pivot separation may be gained through the sequential journal position sketches in Figure 5. Under circular motion, the journal approaches, rests over, and then departs from each pad as illustrated through the sequence of five sketches. The positions of approach and departure are described in the accompanying table, with comparative force magnitudes labeled using integers between -5 and +5. At position 1, the journal approach velocity is maximum and the damping level is intermediate, yielding a comparative damping force (velocity x damping) of +2. Combining this with a low stiffness force of +1 gives a comparative pivot load of +3 at position 1. As the journal precesses toward the pad into position 2, the approach velocity is still high, but the damping is increased by the smaller clearance, yielding a higher damping force of +3. This, combined with a much higher stiffness force of +4 (also due to the smaller clearance), yields the highest comparative pivot load of all at +7. Further precessing the rotor to position 3

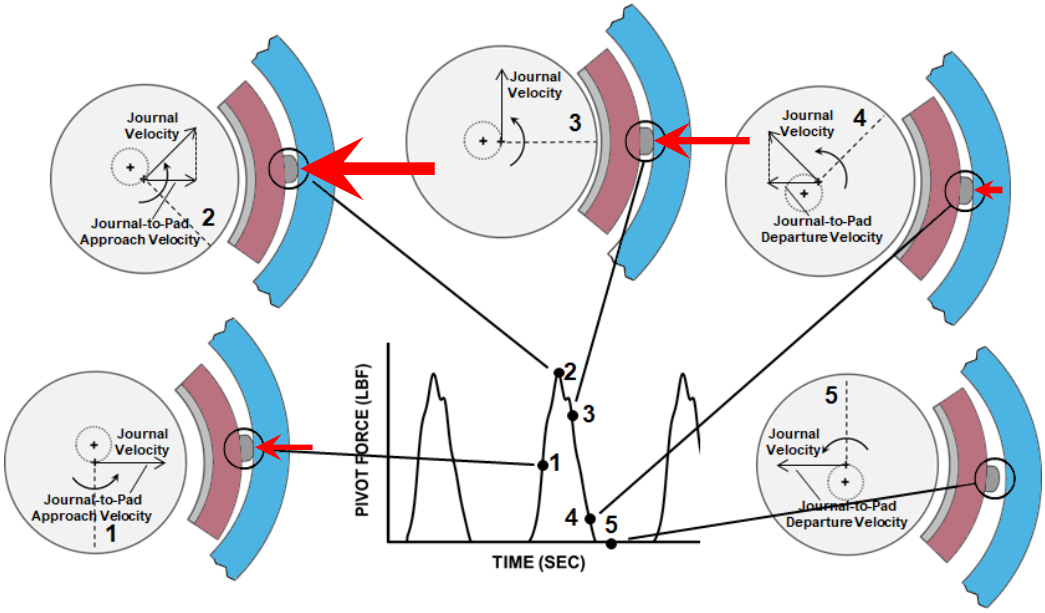

ORBIT POSITION	MOTION	DAMPING-INDUCED PIVOT LOAD (-3 to +3)	POSITION	STIFFNESS-INDUCED PIVOT LOAD (-5 to +5)	TOTAL PIVOT LOAD (-8 to +8)
1	Maximum Approach Velocity	+2	Large Clearance	+1	+3
2	Intermediate Approach Velocity	+3	Intermediate Clearance	+4	+7
3	Stationary	0	Minimum Clearance	+5	+5
4	Intermediate Departure Velocity	-3 (Suction)	Intermediate Clearance	+4	+1
5	Maximum Departure Velocity	-2 (Suction)	Large Clearance	+1	-1 (Separation)

Figure 5. Stages of Journal-to-Pad Approach and Departure

places the journal closest to the pad. Here, the pad approach velocity vanishes and the film is thinnest, yielding zero damping force even though the physical damping is highest. The accompanying stiffness force is maximum due to the thin film, giving a total comparative pivot load of +5. As the journal moves away from the pad to position 4, the same damping and stiffness magnitudes are present as in position 2, but with the damping force reversed due to the departing velocity (fluid suction). This lowers the comparative pivot load to +1, placing it near the threshold of separation. Finally, precession to position 5 where the departure velocity is greatest creates a suction force of -2 that now overcomes the compression force of +1 from stiffness, causing the pivot to separate from the housing and the pad to track the journal. While not shown, the remainder of the orbit is characterized by film refill, where the inflow of lubricant between the pad and journal eventually re-establishes pivot contact and the cycle repeats.

DYNAMIC MODEL

The prediction of large-displacement effects such as pivot separation in tilting-pad bearings requires a scheme capable of representing large motions and system nonlinearities. This requires an iterative solution in the form of either a time-stepping steady-state model, or a full transient solution of the system equations of motion. The current study employs the latter transient approach, in which the journal and pad degrees-of-freedom are solved over many incremental time steps. The nonlinear film and pivot forces are updated each time step using the instantaneous pad position and velocity states.

Pad Equations of Motion

Shown in Figure 6 is a schematic view of a single tilting pad with the film and pivot forces acting on opposite sides. Each pad is assigned a local coordinate system with the coordinates X_P and Y_P that are aligned with the radial and tangential directions, and the axial coordinate Z that is common to all pads. The film hydrodynamic pressure can be resolved into a load passing through the pivot and a moment about the pivot.

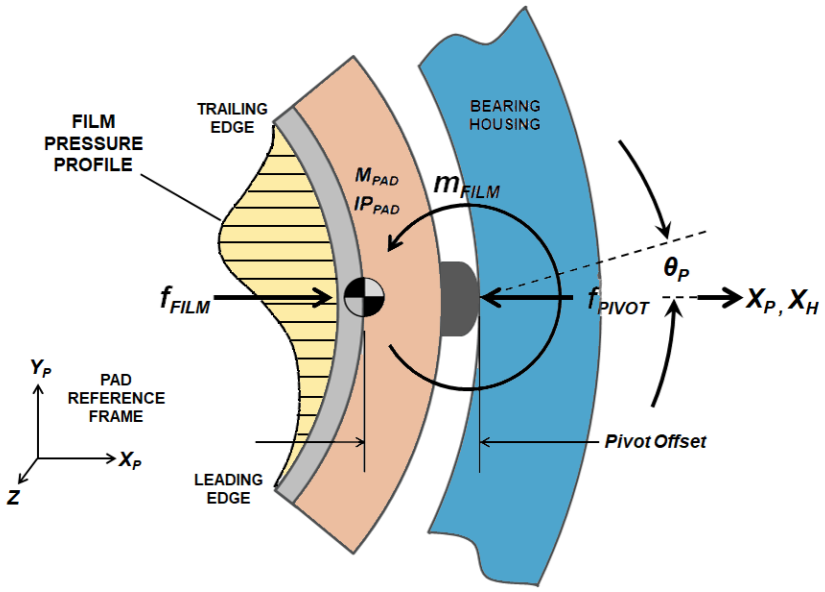

Fig. 6 Pad Coordinate System and Forces

The most convenient origin of reference for solving the pad equations of motion is the point of contact between the pivot and housing. This requires establishing an effective pad rotational inertia as

$$IP_{Eff} = IP_{Pad} + M_{Pad}\ x\ Pivot\ Offset^{\,2} \tag{1}$$

Summing the forces and moments about the pivot gives the pad translational and rotational equations of motion as

$$M_{Pad}\ \ddot{X}_P - f_{Pivot} = f_{Film} \tag{2}$$

$$IP_{Eff}\ \ddot{\theta}_P = m_{Film} \tag{3}$$

If the pivot has a sphere-on-flat geometry, then the pivot force becomes that given for Hertz contact as

$$f_{Pivot} = 0.732\ x\ E\ x\ R_{Pivot}^{0.5}\ (X_P - X_H)^{1.5} \tag{4}$$

where E is the elastic modulus, R_{Pivot} is the spherical pivot radius, and X_H is the instantaneous housing displacement in the direction of

the pivot. After solving Reynolds equation for the hydrodynamic loads as described below, the two pad equations of motion are solved at each incremental time step within the transient solution. Since the pads and films form the physical load path between the bearing housing and the rotor, the pivot force and film force are saved for use in solving the respective housing and rotor equations of motion within the larger rotordynamic model.

Film Loads

Solution of the film hydrodynamic pressures must be achieved with minimal computational effort to become viable in a transient scheme where results are needed at millions of time steps. While most bearing analysis programs incorporate a full two-dimensional Reynolds solution to capture the circumferential and axial pressure variations, such solutions are generally too slow computationally for a transient model. An alternative approach that can give good results is a one-dimensional (1-D) Reynolds solution with an assumed parabolic pressure distribution in the axial direction. Knight and Barrett (Reference 19) incorporated a similar 1-D approach to economize steady-state bearing pressure calculations. If the film is also assumed to be isothermal (isoviscous), eliminating the solution of an energy equation, then an economical solution for pressures can be developed.

Sketched in Figure 7 is a section of converging fluid film divided into a series of five fluid elements. The lower surface is fixed and the upper surface is translating at velocity, *U*, to represent the moving journal surface.

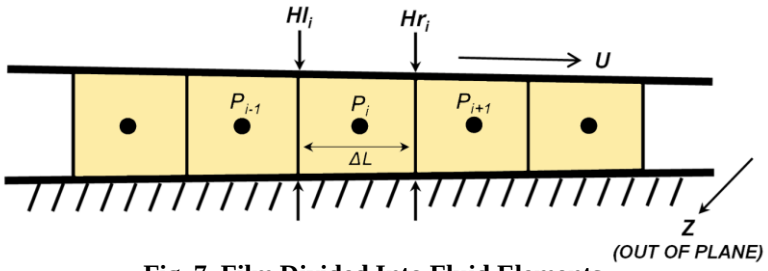

Fig. 7 Film Divided Into Fluid Elements

For solving the film nodal pressures, the Reynolds equation can be reduced to the continuity relationships in Equation 5 for flow through cell i. To satisfy continuity in an incompressible fluid, the sum of the pressure and shear-induced flow into cell i must equal the time rate of change in cell volume from wall closure (squeeze) effects. The two terms on the left express the pressure-induced flow entering and exiting the left and right cell boundaries, respectively. This must equal the sum of the shear flow out plus the volume increase expressed by the terms on the right.

$$\underbrace{\frac{(P_{i-1} - P_i)Hl_i^3\Delta Z}{12\mu_l\Delta L}}_{\text{PRESSURE FLOW IN}} - \underbrace{\frac{(P_i - P_{i+1})Hr_i^3\Delta Z}{12\mu_r\Delta L}}_{\text{PRESSURE FLOW OUT}} = \underbrace{\frac{U}{2}\Delta Z\,(Hr_i - Hl_i)}_{\text{SHEAR FLOW OUT}} + \underbrace{\Delta L\Delta Z * \dot{H}_i}_{\text{TIME RATE OF VOLUME INCREASE}} \tag{5}$$

Assuming a unit length normal to the flow ($\Delta Z = 1.0$), and an isoviscous film ($\mu_l = \mu_r = \mu$), the continuity equation can be simplified to

$$(P_{i-1} - P_i)Hl_i^3 - (P_i - P_{i+1})Hr_i^3 = 12\mu\Delta L\left(\frac{U}{2}(Hr_i - Hl_i) + \Delta L * \dot{H}_i\right) \tag{6}$$

Since the instantaneous boundary film thickness and velocities, H_i and $\dot{H}_i$, are known from the dynamic solution, the right side of Equation 6 can be grouped as a constant. This allows for assembly of the pressure equations in matrix form as shown in Equation 7 for a set of four cells. A tri-diagonal matrix solver provides an expedient solution for the film pressures in terms of the instantaneous film thicknesses, the journal surface velocity, and the film closure rate.

$$\begin{bmatrix} Hl_1^3 + Hl_2^3 & -Hl_2^3 & 0 & 0 \\ -Hl_2^3 & Hl_2^3 + Hl_3^3 & -Hl_3^3 & 0 \\ 0 & -Hl_3^3 & Hl_3^3 + Hl_4^3 & -Hl_4^3 \\ 0 & 0 & -Hl_4^3 & Hl_4^3 + Hl_5^3 \end{bmatrix} \begin{Bmatrix} P_1 \\ P_2 \\ P_3 \\ P_4 \end{Bmatrix} = - \begin{Bmatrix} RHS_1 \\ RHS_2 \\ RHS_3 \\ RHS_4 \end{Bmatrix} \tag{7}$$

Rotordynamic Model

The above pad and film models were incorporated into a larger generalized rotordynamic model for solution of the rotor-bearing dynamic response. The rotordynamic model performs time transient numerical integration of the modal equations of motion with coordinate transformation between physical and modal coordinates at each integration time step. A generic three-level rotordynamic model is illustrated in Figure 8, with the physical tilting pad bearings identified. Outboard of the tilting pad bearings is a lumped-parameter second level that can represent either bearing pedestals or housings, depending on the presence of a third-level casing.

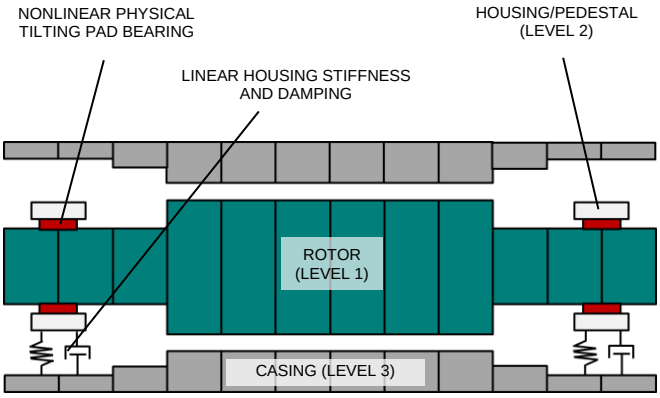

Fig. 8 Three-Level Rotordynamic Model

The general second order differential equations of motion for the rotor-bearing system are expressed in matrix form as

$$[M]\{\ddot{u}(t)\} + [C]\{\dot{u}(t)\} + [K]\{u(t)\} = \{F(t)\} \tag{8}$$

For computation of the real modes, the damping and forcing function are dropped, leaving the undamped homogeneous equation

$$[M]\{\ddot{u}(t)\} + [K]\{u(t)\} = 0 \tag{9}$$

Assuming a solution of the form

$$\ddot{u}(t) = -\omega^2 A e^{i\omega t} = -\omega^2 u(t) \tag{10}$$

then the second derivative becomes

$$\ddot{u}(t) = -\omega^2 u(t) \tag{11}$$

Substituting Equation 11 into the homogeneous equation of motion yields the standard undamped eigenvalue equation as

$$\left[[M]^{-1}[K] - \omega^2 [I]\right]\{\gamma_i\} = 0 \tag{12}$$

where γ_i are the eigenvectors. The orthonormal modes may then be computed as

$$\{\emptyset_i\} = \frac{\{\gamma_i\}}{\sqrt{\gamma_i{}^T [M] \{\gamma_i\}}} \tag{13}$$

The orthogonality conditions for the modes are

$$\{\emptyset_i\}^T[M]\{\emptyset_i\} = \lceil I \rfloor \quad and \quad \{\emptyset_i\}^T[K]\{\emptyset_i\} = \lceil \omega^2 \rfloor \tag{14}$$

Returning to the undamped system equations of motion (Equation 9) and dropping the time dependence, the unbalance forces, support forces, and gyroscopic forces are added on the right side to give the non-homogeneous equations of motion as

$$[M]\{\ddot{u}\} + [K]\{u\} = \{F_{ub}\} + \{F_{sup}\} + \{F_{gyr}\} = \{F\} \tag{15}$$

where

$$\begin{aligned} F_t &= Total\ Force\ Vector \\ F_{ub} &= Unbalance\ Forces \\ F_{sup} &= Support\ Forces \\ F_{gyr} &= Gyroscopic\ Forces \end{aligned}$$

The unbalance forces for any station, *i*, are defined by the unbalance masses, M_{ub}, eccentricity, *e*, and phase angle, ϑ, as

$$\begin{Bmatrix} Fx_{ub} \\ Fy_{ub} \end{Bmatrix}_i = \begin{Bmatrix} M_{ub}\, e\omega^2 \cos(\omega t + \vartheta) \\ M_{ub}\, e\omega^2 \sin(\omega t + \vartheta) \end{Bmatrix}_i \tag{16}$$

The gyroscopic moments for small displacements without rotor acceleration effects are

$$\{F_{gyr}\}_i = \begin{Bmatrix} Mx_{gyr} \\ My_{gyr} \end{Bmatrix}_i = \begin{Bmatrix} -\omega I_p\, \dot{\theta}_y \\ \omega I_p\, \dot{\theta}_x \end{Bmatrix}_i \tag{17}$$

The modal transformation is based on the assumption that the physical responses are expressible as a linear combination of the modal responses transformed by the mode shapes as

$$\{u\} = [\emptyset]\{q\} \tag{18}$$

Substituting this transformation into Equation 15 yields

$$[M][\emptyset]\{\ddot{q}\} + [K][\emptyset]\{q\} = \{F\} \tag{19}$$

Pre-multiplying both sides by the transpose of the mode shapes gives

$$[\emptyset]^T[M][\emptyset]\{\ddot{q}\} + [\emptyset]^T[K][\emptyset]\{q\} = [\emptyset]^T\{F\} \tag{20}$$

Substituting the orthogonality relations of Equation 14 yields the uncoupled modal equations of motion as

$$\{\ddot{q}\} + [\omega^2]\{q\} = \{f\} \tag{21}$$

where $\{f\}$ is now the modal force vector after transformtion to modal coordinates. Since the modes remain uncoupled, the modal equations may be solved individually. It is common to include the effects of material damping in the rotor through a modal damping term, ζ_i, for each mode to yield

$$\ddot{q}_i + 2\omega_i\, \zeta_i\, \dot{q}_i + \omega_i^2\, q_i = f_i \tag{22}$$

This is the form of the modal equations which are solved by transient numerical integration with the tilting pad bearing forces transformed into the modal force vector, f_i, at each integration time step.

CASE STUDY – OVERHUNG COMPRESSOR

History

A centrifugal plant air handling compressor (Figure 9) running 24 hr/day in the field was experiencing frequent machine outages due to excessive bearing pivot wear. The compressor geometry and operating parameters are listed in Table 2. The machine is a single-stage, overhung, centrifugal blower typical of many machines in service throughout the petrochemical, manufacturing, and mining industries. In this particular application, the impeller would become unbalanced over time through abrasive erosion. As the unbalance increased, the bearing dynamic loads would fatigue the pad pivots on the rocker-pivot tilting pad bearings, causing excessive bearing clearances that would raise the vibration levels and trip the machine off line. Frequent (approximately every three months) bearing overhauls were required to keep the machine operational. Because of the persistent reliability problems with the compressor, the customer was interested in upgrading the machine beyond the conventional "patch up" type of repair. Rather, he was seeking a comprehensive reanalysis and redesign that would permanently correct the vibration problems and eliminate the costly outages.

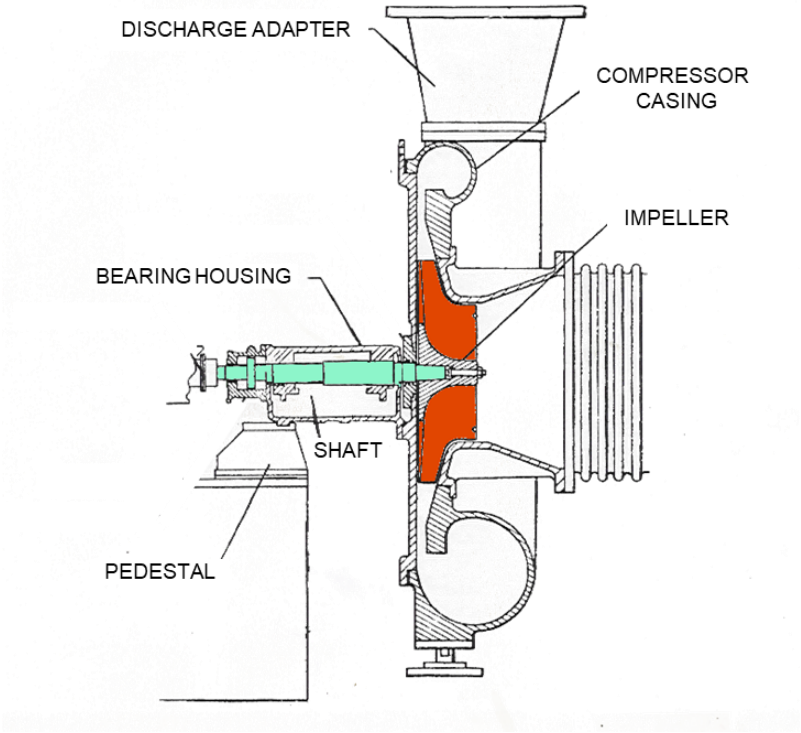

Figure 9. Compressor Layout

Table 2. Compressor Design and Operating Conditions

Running Speed	6,300.0 rpm
Rated Power	3,500.0 hp
Rotating Weight	625.0 lbm
Impeller Diameter	39.5 in
Bearing Span	17.5 in

Early Design Upgrades

Upon engagement by the customer in 1987, the author performed a linear rotor-bearing dynamic analysis that is documented in References 17 and 18. Conclusions from that analysis were that a reduction in shaft stiffness would be beneficial in reducing the bearing loads by shifting the first bending mode farther below running speed. This led to reducing the shaft diameter between the bearings from 5.5 in to 2.8 in as illustrated along with the respective undamped critical speed mode shapes in Figure 10. In calculating the undamped critical speeds, approximate bearing dynamic stiffnesses of 350,000.0 lbf/in and 450,000.0 lbf/in were applied at the drive and impeller end bearings, respectively. The smaller shaft reduces the first and second undamped critical speeds by approximately 21.0 % and 27.0 %, respectively. Plotted in Figure 11 are the calculated speed-varying bearing loads for the original and reduced-diameter shafts with a 4.5 oz-in unbalance placed at the impeller. At the 6300.0 rpm running speed, the bearing dynamic loads are reduced by approximately 48.0 % and 72.0 % at the impeller end and coupling end, respectively, relative to the original rigid-shaft design. Without any bearing changes, these reductions alone would be expected to significantly improve the service life for a given trend of increasing impeller unbalance.

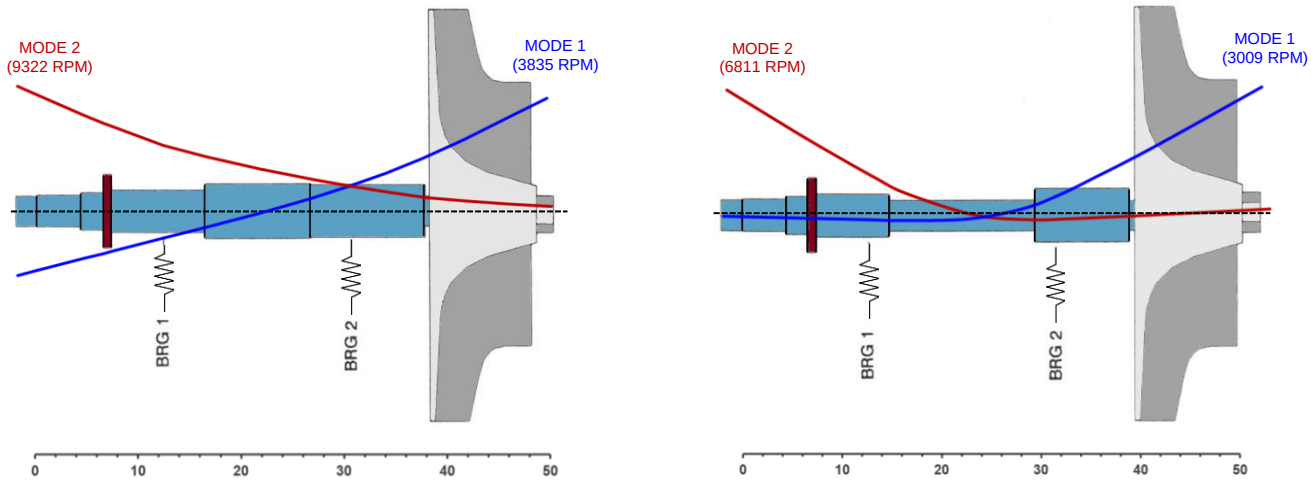

Figure 10. Undamped Critical Speed Mode Shapes of Original and Reduced-Diameter Rotors

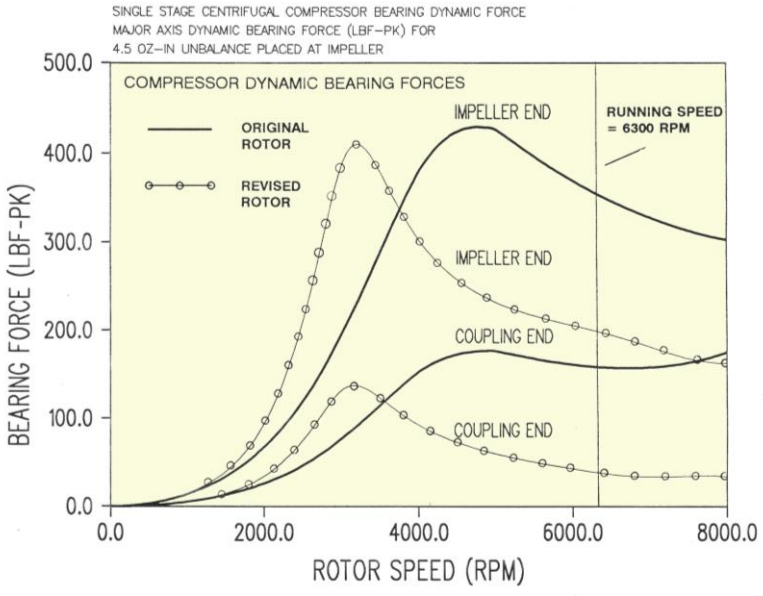

Figure 11. Computed Bearing Dynamic Loads Before and After Rotor Diameter Reduction

Even though the above shaft modifications alone appeared promising, an additional upgrade was implemented by replacing the original rocker-pivot tilting pad bearings with bearings having spherical pivots as shown in Figure 12. The rationale for switching to spherical pivots was in their ability to reduce the contact stresses by almost a factor of 10 relative to the original rocker pivot bearings as shown in Figure 13. This is due to the much larger contact area of a precision- ground ball-in-socket interface compared to that of a standard rocker pivot having a much smaller Hertzian contact surface.

The combination of reducing the bearing dynamic loads and switching to spherical-pivot tilting pad bearings proved to be remedial to the machine reliability issues in 1987. Following the above design changes, the compressor operated continuously for a full year, after which a routine annual inspection revealed no increase in bearing clearances. The machine was re-assembled using the original parts and continued to provide excellent service thereafter.

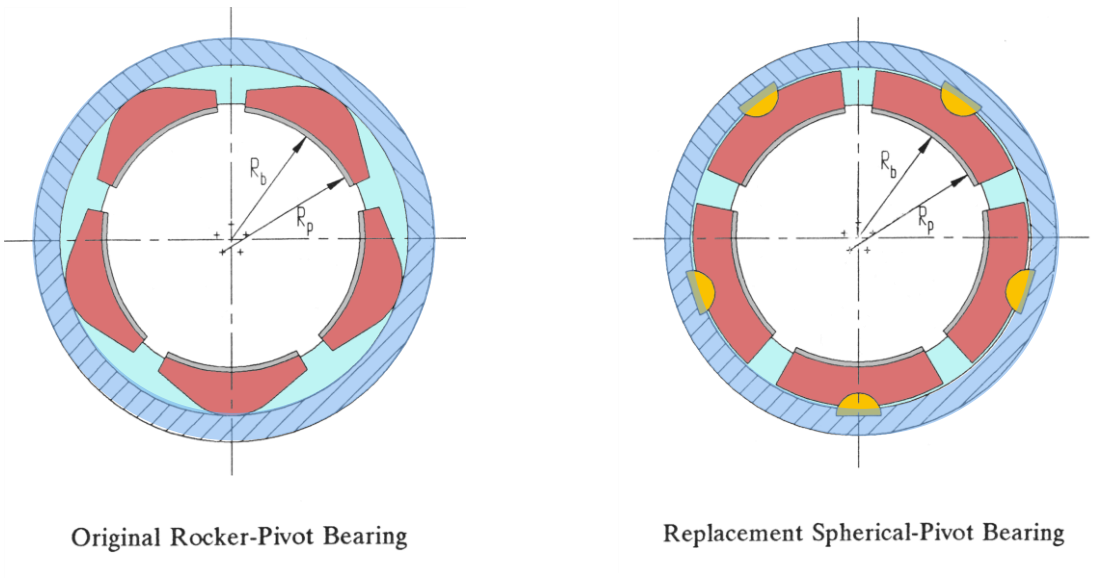

Figure 12. Original Rocker-Pivot and Replacement Spherical-Pivot Bearings

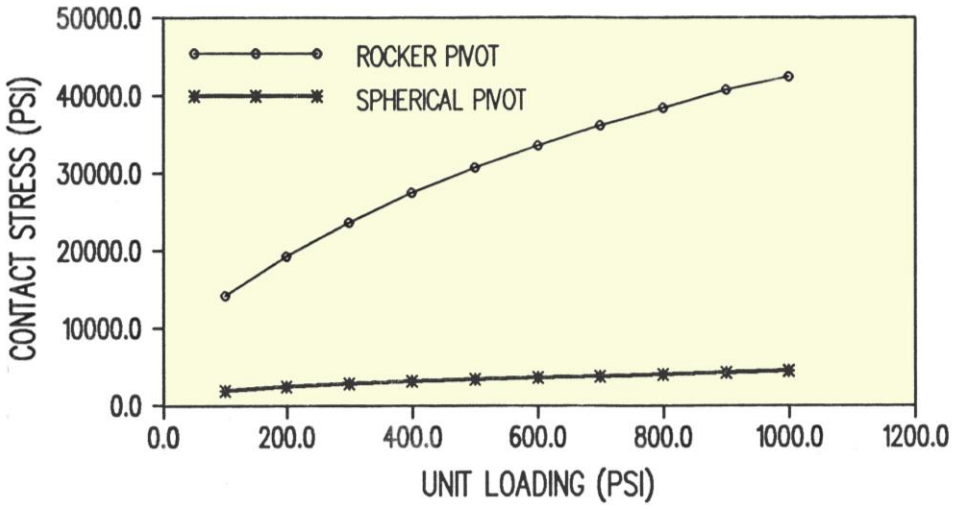

Figure 13. Hertzian Contact Stresses in Rocker versus Spherical Pivots

New Insights into an Old Problem

While the above shaft and bearing improvements were sufficient for the customer's needs approximately 35 years ago, it was suspected that the underlying mechanism compromising the original machine performance was not fully understood. Summarized below are predictions from the new nonlinear model of the bearing behavior in the original problematic design, the revised (remedial) design, and a hypothetical design having a modified bearing geometry.

Rotordynamic Model

To study the potential for nonlinear bearing behavior in the original compressor, a new rotordynamic model was constructed using the nonlinear tilting pad bearing scheme described above. Shown in Figure 14, the model consists of a rotor supported in two bearings with the overhung impeller attached outboard. Supporting the rotor are physical representations of the original tilting pad bearings having the design and operating properties listed in Table 3. Both bearings are of a 5-pad, load-between-pad, configuration with circumferentially centered pivots. Because the heavy impeller is positioned outboard of the bearings, the coupling-end bearing is negatively loaded with an upward load of approximately 145.0 lbf, while the impeller-end bearing carries a downward load of 770.0 lbf. Outboard of the bearings is a rudimentary model of the bearing housing and casing to approximate the non-rotating structure. Estimated support stiffnesses of 5.0 x 10^6 lbf/in connect the casing to ground at opposite ends of the machine. In parallel with the support stiffnesses are estimated damping values of 1000.0 lbf-sec/in to approximate support damping in a diffuser-casing weighing approximately 50,000.0 lbm.

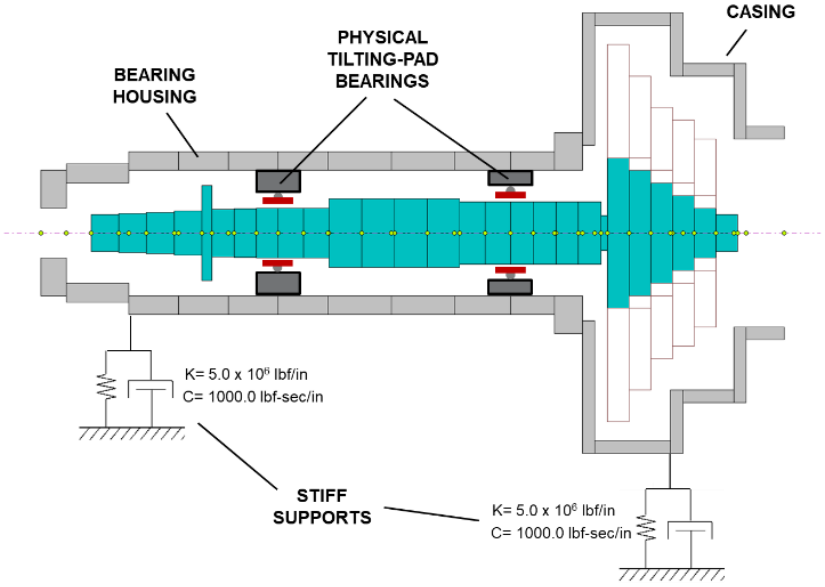

Figure 14. Nonlinear Rotordynamic Model with Original Rotor

Table 3. Original Bearing Parameters

	IMPELLER END	COUPLING END
BEARING TYPE	5-Pad Tilting Pad Load Between Pad	5-Pad Tilting Pad Load Between Pad
JOURNAL DIAMETER	5.0 in	4.0 in
AXIAL LENGTH	3.5 in	2.8 in
PAD ARC	68.0 deg	68.0 deg
RADIAL SET CLEARANCE	3.5 mils	4.0 mils
PREOAD	0.3	0.0
PIVOT OFFSET	0.5	0.5
STATIC LOAD	770.0 lbf	-145.0 lbf
OIL TYPE	150 SSU @ 150 F	150 SSU @ 150 F

Original Rotor and Bearings

The nonlinear model was first exercised to simulate a startup event in the original machine, where the speed was gradually ramped up from 500.0 rpm to about 10% above the 6300.0 rpm running. Hereinafter, loads and journal motions will be presented for the impeller-end bearing only, as these are typically the highest of the two bearings and are, therefore, bounding. The calculated impeller-end bearing response and dynamic loads are plotted in Figures 15 and 16 for four levels of impeller unbalance ranging from a modest 5.0 oz-in, up to a very severe unbalance of 20.0 oz-in. When the impeller unbalance is limited to 10.0 oz-in and below, the response remains substantially linear, rising up to a first mode peak at around 4000.0 rpm to 4300.0 rpm. The response then falls off as the critical speed is traversed. In contrast, when the unbalance is increased to 15.0 oz-in and above, the bearing enters a nonlinear regime where a very interesting phenomenon ensues. Nonlinear bearing stiffening under the higher journal motion elevates the critical speed in parallel with the increasing running speed until a point of multiple solutions. Under the 20.0 oz-in impeller unbalance, the critical speed continues

to track running speed up to a point of dynamic instability at about 5800.0 rpm, after which a nonlinear jump occurs as the critical speed cannot escalate further and suddenly drops back down below running speed. During the nonlinear escalation, degradation of bearing damping causes violent motions with very high dynamic bearing loading reaching as high as 50,000.0 lbf-pk under the 20.0 oz-in unbalance.

It is clear from these results that if the original compressor became unbalanced enough to encounter nonlinear vibration escalation during startup as severe as that predicted for the 20.0 oz-in impeller unbalance, the mechanical integrity would have been jeopardized unless a vibration trip was able to intercede. Since the machine never failed catastrophically, it clearly tripped off line before such high unbalance and vibration levels were ever reached.

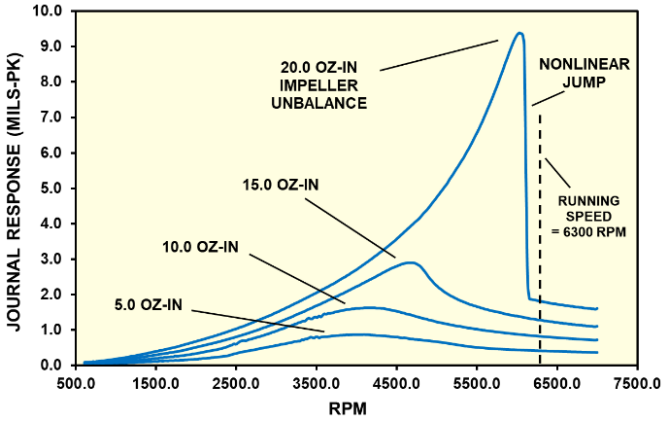

Figure 15. Computed Impeller-End Journal Response at Four Unbalance Levels During Compressor Startup - Original Rotor and Bearings

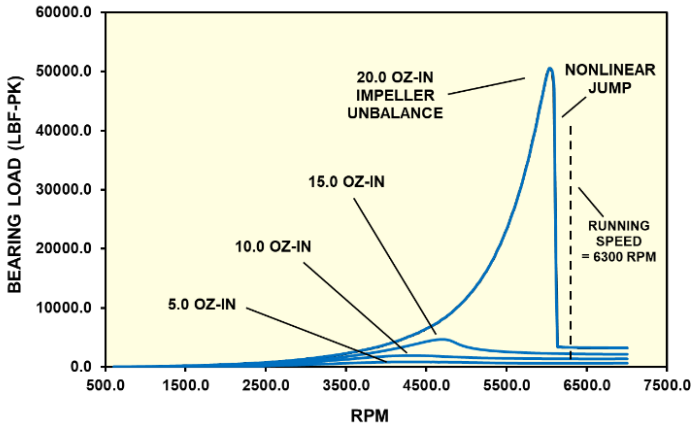

Figure 16. Computed Impeller-End Bearing Dynamic Load at Four Unbalance Levels During Compressor Startup - Original Rotor and Bearings

As a graphical summary of the above system nonlinearities, the variations in critical speed, peak impeller end journal response, and peak impeller end dynamic bearing load with impeller unbalance are plotted in Figure 17. The rising critical speed with unbalance, which would remain stationary in a linear system, reflects nonlinear stiffening of the bearing films with whirl amplitude. Similarly, the exponentially-increasing journal motions and bearing loads, which would vary linearly with unbalance in a linear system, also evidence the highly nonlinear bearing characteristics.

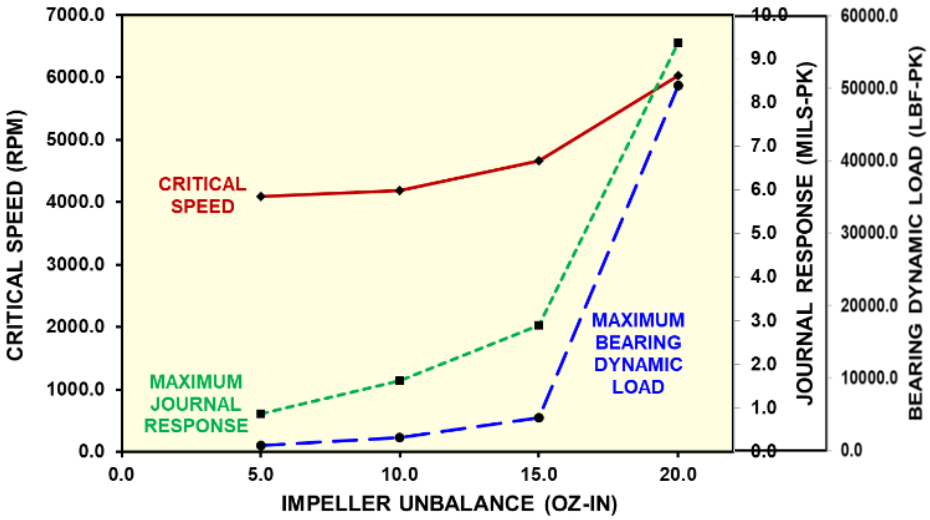

Figure 17. Critical Speed, Impeller End Maximum Journal Response, and Impeller End Maximum Bearing Load versus Impeller Unbalance - Original Rotor and Bearings

To observe the running-speed orbit characteristics, the model was held at the 6300 rpm running speed while driven by a 20.0 oz.-in impeller unbalance. The resulting impeller-end journal whirl orbit and pivot loads are plotted in Figure 18. The orbit occupies about 60% of the bearing clearance and the pivot loads reach as high as 2840.0 lbf-pk at Pivot 5. All five pads exhibit brief pivot separation, with more severe unloading in the lightly load pads (Pads 1-3).

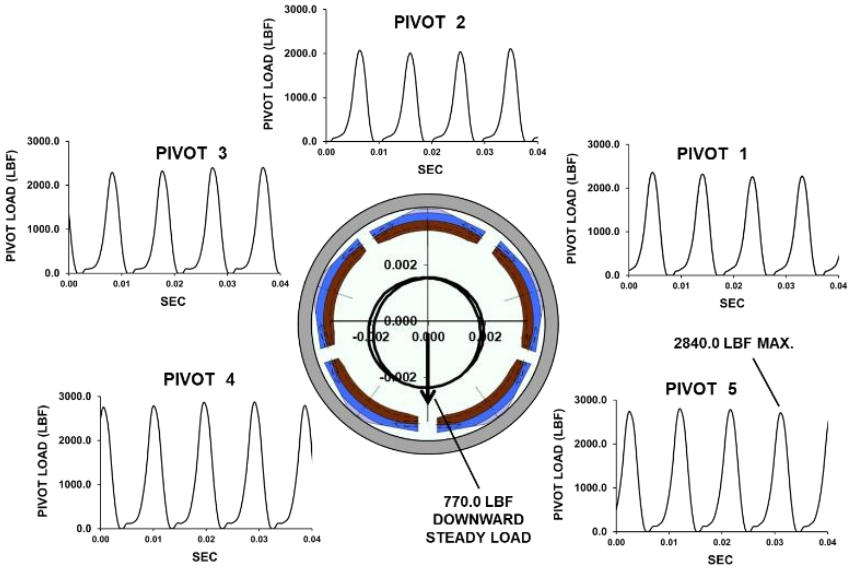

Figure 18. Computed Impeller-End Journal Orbit and Pivot Loads at 6300.0 rpm Under 20.0 oz-in Impeller Unbalance - Original Rotor and Bearings

Reduced-Diameter Rotor - Original Bearings

To observe the effects of the redesigned shaft on the dynamic behavior, the above startup analysis was repeated with the revised shaft supported in the original tilting pad bearings. In the current study, both the rocker pivot and modified ball-and-socket pivot bearings are considered "original" bearings, as no changes were made to clearances, preload, or pad orientations. Illustrated in Figure 19 is the modified-shaft model having bearing and casing properties similar to model above, but with the shaft diameter reduced to 2.8 inches between the bearings.

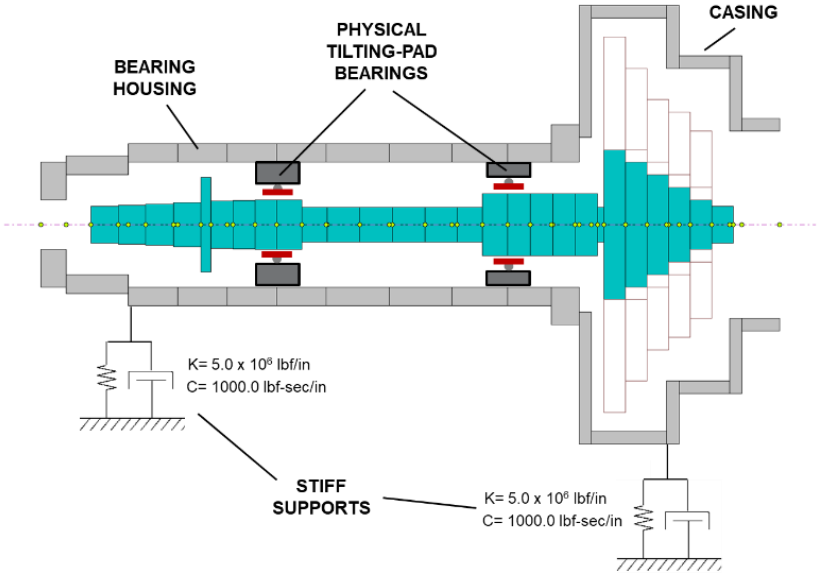

Figure 19. Nonlinear Rotordynamic Model with Reduced-Diameter Rotor

The computed impeller-end bearing response and dynamic loads with the smaller shaft are plotted in Figures 20 and 21 for the same four levels of impeller unbalance analyzed above. As with the original shaft, when the impeller unbalance is limited to 10.0 oz.-in and below, the response remains substantially linear, rising up to the first mode peak that is now around 2600.0 rpm, and then falling off as the critical speed is traversed. However, the nonlinear vibration escalation still ensues at the two higher unbalances, albeit not quite as severely as with the original large shaft. Compared to the original design, the maximum journal amplitude with a 20.0 oz-in unbalance is reduced about 37%, from 9.5 mils-pk to around 6.0 mils-pk. The peak bearing load is reduced about 65% from 50,000.0 lbf-pk to 17,500.0 lbf-pk. In Figure 22, showing the variation of peak values with unbalance, the softer shaft has yielded more linear behavior as evidenced by the nearly-stationary critical speed. The journal response and bearing loads now rise less sharply with unbalance.

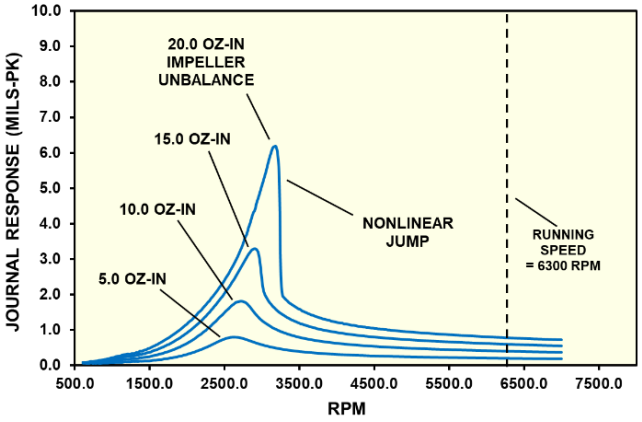

Figure 20. Computed Impeller-End Journal Response at Four Unbalance Levels During Compressor Startup; Reduced-Diameter Rotor with Original Bearings

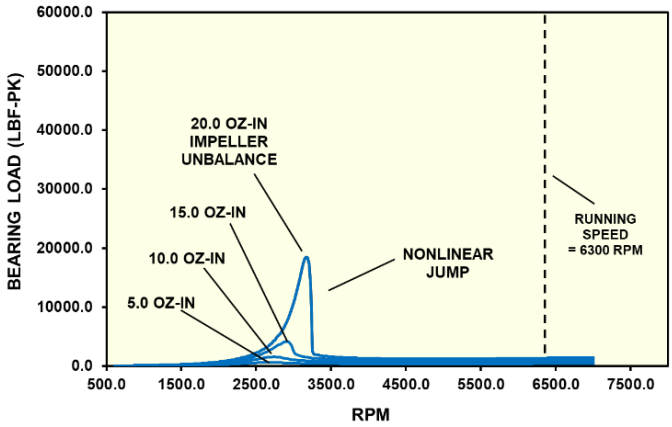

Figure 21. Computed Impeller-End Bearing Dynamic Load at Four Unbalance Levels During Compressor Startup – Reduced-Diameter

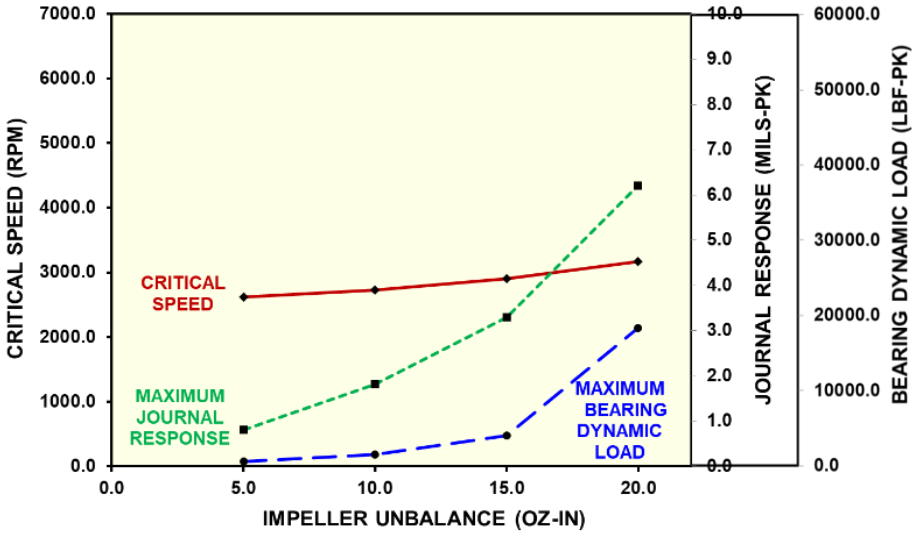

Figure 22. Critical Speed, Impeller End Maximum Journal Response, and Impeller End Maximum Bearing Dynamic Load versus Impeller Unbalance - Reduced-Diameter Rotor with Original Bearings

The computed whirl orbit and pivot loads during steady operation at 6300.0 rpm are plotted in Figure 23 for the highest unbalance of 20.0 oz-in. Unlike the earlier results in Figure 18 for the larger shaft, the pivots now remain in contact with the housing at all five pad locations. The orbit now occupies only about 30% of the bearing clearance, yielding approximately a 50% reduction in running-speed journal amplitude compared to that with the original shaft.

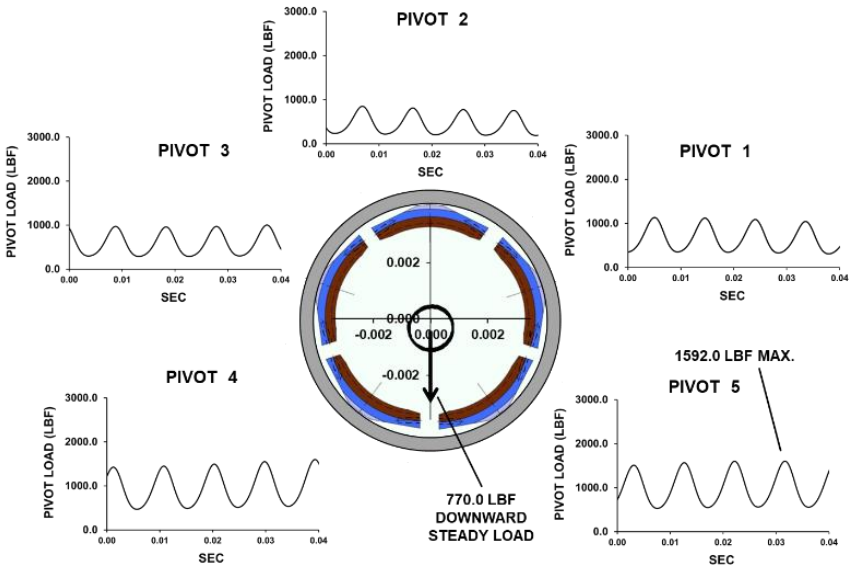

Figure 23. Computed Impeller-End Journal Orbit and Pivot Loads at 6300.0 rpm Under 20.0 oz-in Impeller Unbalance – Reduced-Diameter Rotor with Original Bearings

These noted improvements are reflective of the downward shift in critical speed afforded by the more flexible shaft. They are also consistent with the machine reliability improvements following the shaft modifications. It is clear why shaft stiffness reductions, in combination with improvements to the bearing pivot design, were successful in meeting the immediate needs of the customer 35 years ago. However, the above results also show that the shaft changes alone were not sufficient to suppress the potential for violent motions during startup if the impeller became severely unbalanced. As with the original shaft, it is likely that the compressor either did not become as severely unbalanced as assumed in upper limits of the current examples, or that plant monitoring was able to intercede before damage occurred. It should be emphasized that the unbalance levels of 15.0 oz-in and 20.0 oz-in assumed for the current study were intentionally set very high to emphasize the effects of bearing nonlinearity should the unbalance reach such levels.

Alternate Bearings

In search of bearing improvements that could reduce both the steady state vibration at the 6300 rpm running speed as well as the potential for nonlinear escalation at startup, a range of bearing modifications was investigated using the nonlinear bearing model. After a parametric study that varied the number of pads, pad axial length, radial clearance, preload, and edge treatments, an alternate design was evolved having the parameters listed in Table 4. Those of the original bearings are also shown for comparison. The primary goal was to raise the effective bearing damping by lowering the stiffness and maintaining the physical damping. This was achieved by switching from five to four pads and raising the radial clearance of both bearings to 6.0 mils from the original clearances of 4.0 mils and 3.5 mils at the coupling and impeller end bearings, respectively. The pad axial lengths were also raised from 2.8 inches and 3.5 inches to 4.0 inches and 5.0 inches at the coupling and impeller ends, respectively. Longer pads tend to lower stiffness by making the journal more centered in the bearing, while also increasing damping by increasing the surface area. In place of a preload, edge tapers measuring 5.0 degrees by 0.005 inches depth were added at the pad leading and trailing edges of both bearings. Shown schematically in Figure 24, the aggressive convergence introduced by edge tapers raises the average pressure across the entire film. Studies by the author have shown that edge tapers prevent pad and pivot unloading more effectively than a preload geometry when the journal migrates away from the lightly loaded pads. By leaving the interior portion of the pad concentric with the journal, edge tapers also tend to increase squeeze film effects, leading to higher film damping.

Table 4. Original and Alternate Bearing Designs

	IMPELLER END			COUPLING END	
	ORIGINAL BEARING	ALTERNATE BEARING		ORIGINAL BEARING	ALTERNATE BEARING
BEARING TYPE	5-Pad Tilting Pad Load Between Pad	4-Pad Tilting Pad Load Between Pad		5-Pad Tilting Pad Load Between Pad	4-Pad Tilting Pad Load Between Pad
JOURNAL DIAMETER	5.0 in	5.0 in		4.0 in	4.0 in
AXIAL LENGTH	3.5 in	5.0 in		2.8 in	4.0 in
PAD ARC	68.0 deg	80.0 deg		68.0 deg	80.0 deg
PIVOT OFFSET	0.5	0.5		0.5	0.5
RADIAL SET CLEARANCE	3.5 mils	6.0 mils		4.0 mils	6.0 mils
PRELOAD	0.3	0.0		0.0	0.0
EDGE TAPERS	-	5.0 deg x 0.005 in		-	5.0 deg x 0.005 in
STATIC LOAD	770.0 lbf	770.0 lbf		-145.0 lbf	-145.0 lbf

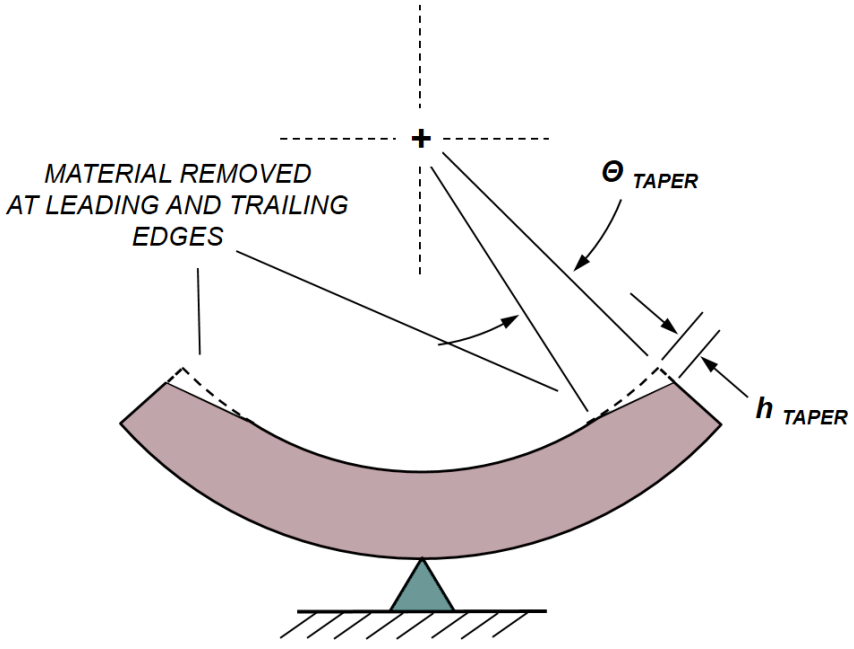

Figure 24. Pad Edge Tapers

Plotted in Figures 25 through 27 are the computed dynamic coefficients and minimum film thicknesses versus speed for both the original and alternate bearings. Because of their larger clearances combined with the longer pads, the alternate bearings have significantly lower stiffness than the original bearings. Even though the physical damping is less affected, the available damping is higher because of the higher journal motion allowed by the lower stiffness. The vertical and horizontal stiffnesses are also equal in the alternate bearing, reflecting the symmetry of a four-pad bearing compared to a five-pad bearing. The higher load capacity of the alternate bearings is reflected through the increased film thicknesses in Figure 27.

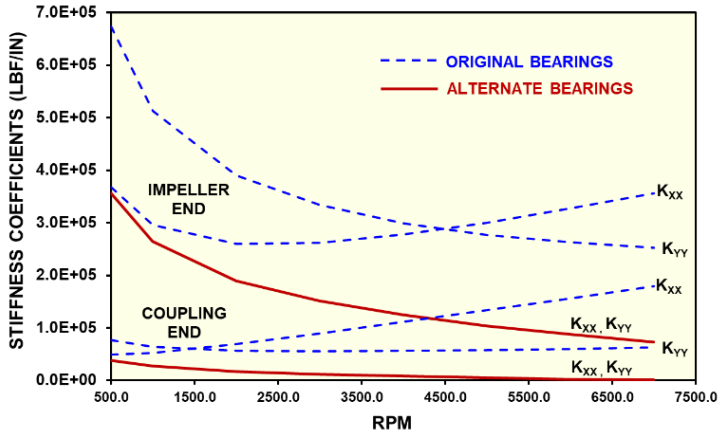

Figure 25. Original and Alternate Bearing Stiffness Coefficients

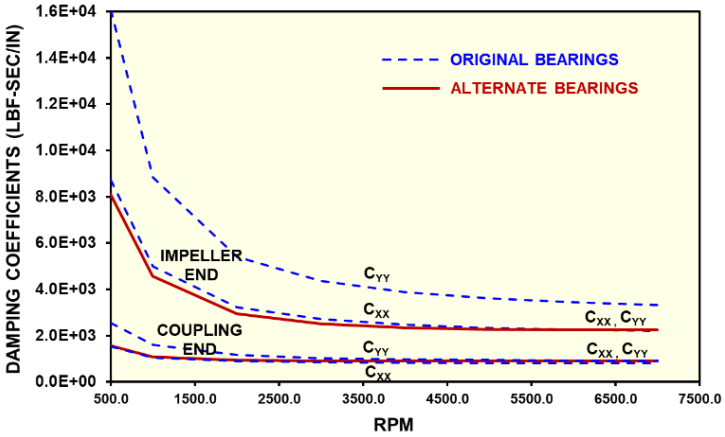

Figure 26. Original and Alternate Bearing Damping Coefficients

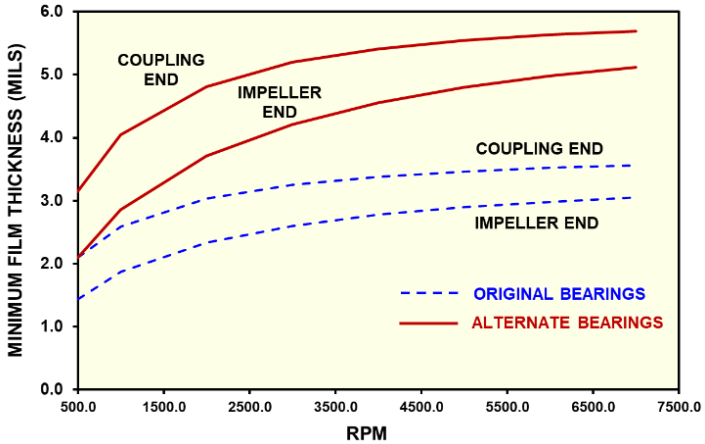

Figure 27. Original and Alternate Bearing Minimum Film Thickness

Computed impeller-end bearing response and dynamic loads with the alternate bearings and flexible shaft are plotted in Figures 28 through 30 for the same four levels of impeller unbalance analyzed earlier. Compared to the prior results with the original bearings, the response is now more linear and without jumps for all excitation levels, including the highest unbalance of 20.0 oz-in. While the journal amplitudes at the 6300.0 rpm running speed are slightly higher in Figure 28 than those in Figure 20 with the original bearings and smaller shaft, the resulting bearing loads are nearly identical to those in the original bearings. This is because the softer films of the larger-clearance bearings allow higher journal motions without an increase in dynamic load. In Figure 30 showing the variation of peak values with unbalance, the behavior is now completely linear as evidenced by the stationary critical speed along with linear increases in journal motion and bearing load. The computed whirl orbit and pivot loads during steady operation at 6300.0 rpm are plotted in Figure 31 for the highest unbalance of 20.0 oz-in. The pivots continue to remain in contact with the housing at all four pad locations, reflecting the low bearing dynamic loads combined with beneficial internal loading from the edge tapers. While the absolute journal response is about 30% greater than that with the original bearings (1.3 mils-pk vs 1.0 mil-pk), it occupies a lower percentage (22% vs 30%) of the now-larger clearance.

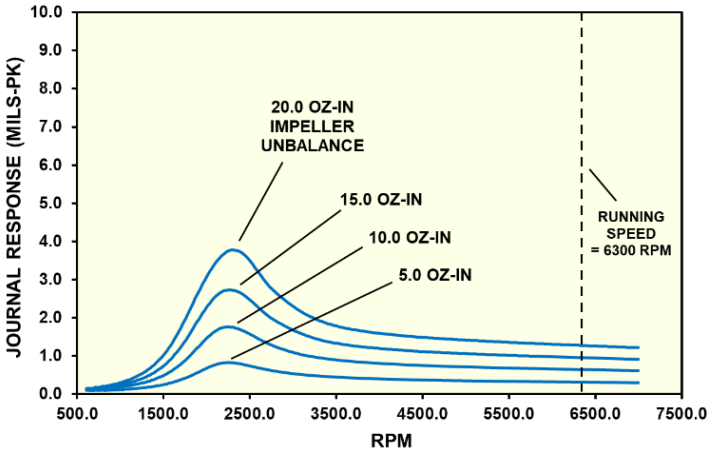

Figure 28. Computed Impeller-End Journal Response at Four Unbalance Levels During Compressor Startup - Reduced-Diameter Rotor with Alternate Bearings

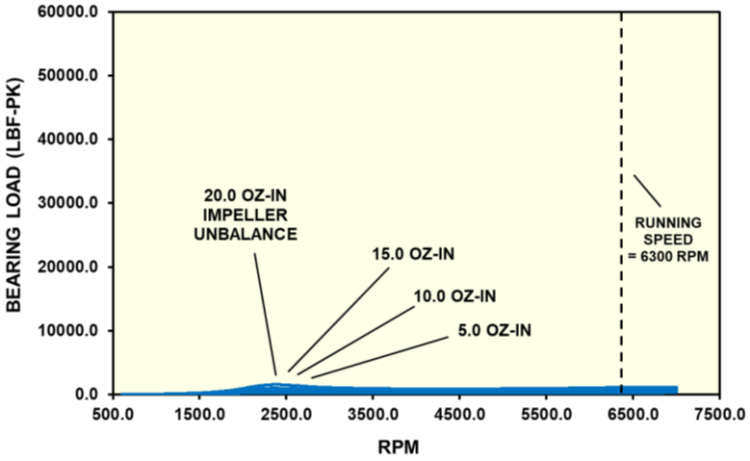

Figure 29. Computed Impeller-End Bearing Dynamic Load at Four Unbalance Levels During Compressor Startup – Reduced-Diameter Rotor with Alternate Bearings

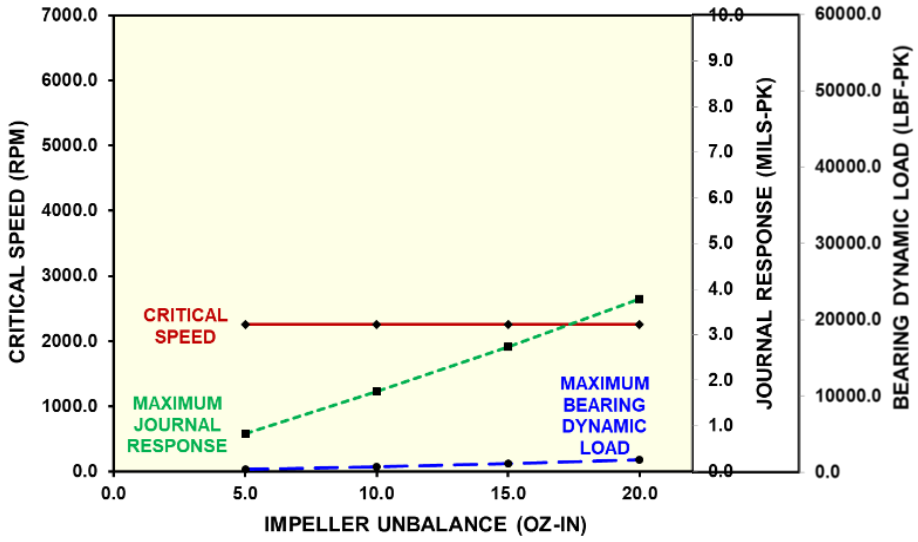

Figure 30. Critical Speed, Impeller End Maximum Journal Response, and Impeller End Maximum Bearing Load versus Impeller Unbalance - Reduced-Diameter Rotor with Alternate Bearings

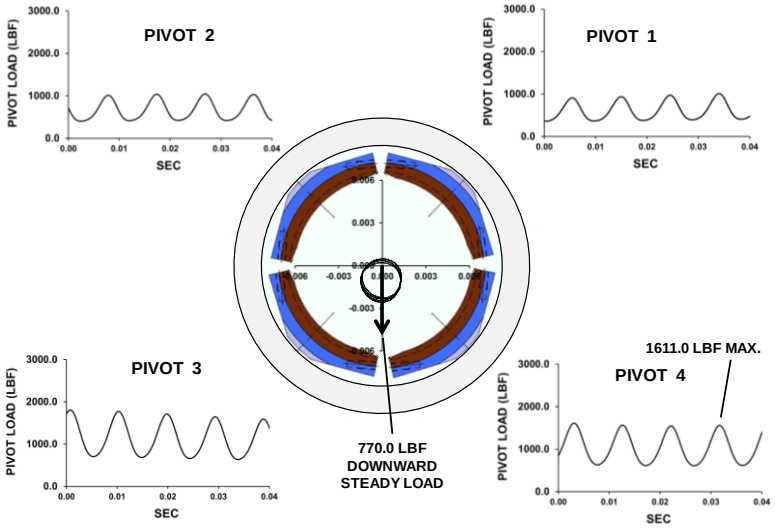

Figure 31. Impeller-End Journal Orbit and Pivot Loads at 6300.0 RPM Under 20.0 oz-in Impeller Unbalance – Reduced-Diameter Rotor with Alternate Bearings

Performance Summary

Limiting the magnitude and variation of tilting pad bearing pivot loads is important for minimizing pivot wear and the potential for bearing clearance changes over time. Ideally, the pivot loads should be of low magnitude and always remain positive to avoid impacting against the housing. To summarize the relative performance of the three machine configurations studied herein, maximum and minimum pivot loads are plotted versus speed in Figures 32 and 33, respectively, for a large impeller unbalance of 20.0 oz-in. In Figure 32, the shaft stiffness reduction alone reduces the computed peak pivot load by about 55.0 %, from 38,890.0 lbf-pk to 17,450.0 lbf-pk. In Figure 33, the smaller journal orbits afforded by the shaft change lower the range of pivot unloading by more than a factor of two, from 50.0 % to 24.0 % of the plotted speed range. These reductions in calculated pivot loads and unloading highlight the intended improvements from the smaller shaft that were ultimately substantiated through the improved machine reliability. An even greater reduction in pivot load is reflected by the solid green curve in Figure 32, where incorporating the alternate bearing configuration discussed above affords an additional factor of 9.0 reduction in computed peak pivot load, from 17,450.0 lbf-pk with just the shaft changes, to 1943.0 lbf-pk with the added bearing modifications. At the 6300 rpm operating speed, the dynamic loads are similar to the those with just the shaft changes, but are about 40 % below those of the original machine. In Figure 33, the alternate bearings are shown to reduce the duration of pivot unloading to only about 3.0% of the plotted speed range, almost completely eliminating pivot separation. While the alternate bearings remain conceptual because they were never implemented in the subject machine, these results suggest that they would reduce the potential for accelerated pivot wear beyond that of the shaft modifications alone. Should a similar overhung compressor exhibit problems with tilting pad bearing longevity, augmenting the prior shaft stiffness reductions with the bearing modifications developed herein would be expected to yield even greater success than that achieved with the shaft changes alone. A potential benefit for the end user would be improved tolerance of impeller unbalance and consequent extension of service outage intervals for impeller re-balancing.

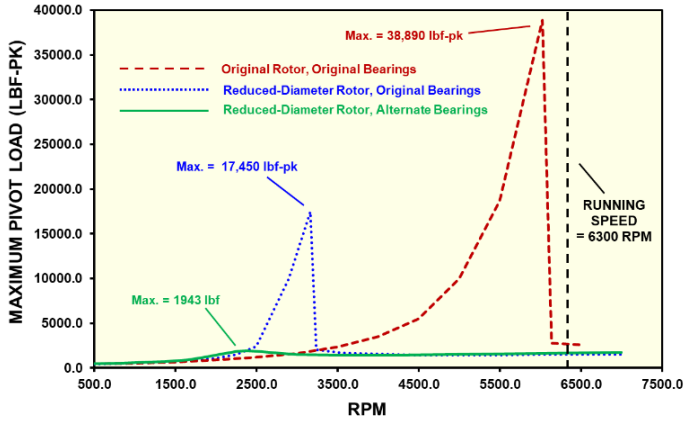

Figure 32. Maximum Impeller-End Pivot Load versus Speed with 20.0 oz-in Impeller Unbalance

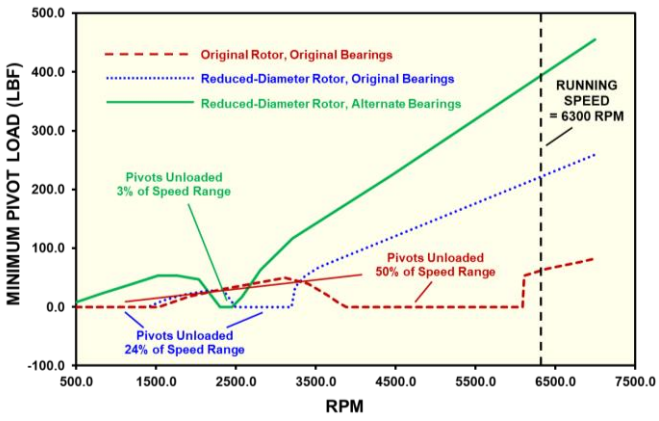

Figure 33. Minimum Impeller-End Pivot Load versus Speed with 20.0 oz-in Impeller Unbalance

CONCLUSIONS

As a result of the current investigation, the following conclusions are reached:

- Prediction of nonlinear effects in tilting pad bearings experiencing high-amplitude journal whirl requires a transient model such as that presented herein, having physical representations of the bearing pads coupled to hydrodynamic solutions of the films that are solved at many incremental time steps.

- If journal whirl amplitudes in machines having tilting pad bearings become large enough to occupy more than about 50% of the bearing clearance, pivot unloading ("rattle") can ensue that leads to accelerated bearing wear and loss of machine reliability. Film nonlinearities associated with high journal motions can also elevate the critical speed and vibration amplitudes exponentially with increasing unbalance, potentially leading to very high bearing loads with sudden nonlinear jumps from high to low vibration levels.

- Inclusion of the current nonlinear bearing model in a rotordynamic analysis of a single-stage overhung compressor produced results confirming the benefits of shaft stiffness reductions developed approximately 35 years ago using a rudimentary linear analysis.

- Exploration of alternative bearing geometries using the nonlinear bearing model led to an alternate set of bearings having four pads in place of the original five, greater axial lengths, larger radial clearances, and leading and trailing edge tapers. Re-analysis of the nonlinear model using the alternate bearings led to the following observations:

    - The alternate bearings, along with the modified shaft, are predicted to eliminate nonlinear jumps and reduce the peak bearing loads during machine startup by up to a factor of nine compared to the original bearings and modified shaft.

    - The increased effective damping and more consistent internal film loading from the use of edge tapers in place of the original preload is predicted to reduce the range of pivot unloading from around 24.0% of the speed range with the original bearings and modified shaft, to only about 3.0% of the operating speed range with the alternate bearings and modified shaft.

    - While the alternate bearings developed herein remain conceptual because they were not implemented in the subject machine, the current results suggest that they would reduce the potential for accelerated pivot wear and high vibration even more effectively than the shaft modifications implemented 35 years ago. A potential benefit for the end user would be improved tolerance of impeller unbalance and consequent extension of service outage intervals for impeller re-balancing.

NOMENCLATURE

C = damping (lbf-sec/in)
E = modulus of elasticity (lbf/in^2)
e = unbalance eccentricity (in)
F = physical force (lbf)
f = modal force (dim)
f_{film} = film radial force (lbf)
f_{pivot} = pivot force (lbf)
Hl = cell left boundary film thickness (in)
Hr = cell right boundary film thickness (in)
Ip = shaft rotational inertia ($lbm\text{-}in^2$)
Ip_{eff} = effective pad rotational inertia ($lbm\text{-}in^2$)
Ip_{pad} = pad rotational inertia ($lbm\text{-}in^2$)
K = stiffness (lbf/in)
L = coordinate parallel to flow
M = mass (lbm)
M_{pad} = pad mass (lbm)
M_{ub} = unbalance mass (lbm)
Mx_{gyr} = x-direction gyroscopic moment (lbf-in)
My_{gyr} = y-direction gyroscopic moment (lbf-in)
m_{film} = film moment (lbf-in)
P = fluid static pressure (lbf/in^2)
q = modal displacement (dim)
R_{pivot} = pivot spherical radius (in)
X_H = housing radial displacement (in)
X_P = pad radial displacement (in)
θ_p = pad angular displacement (rad)
u = physical displacement (in)
U = journal surface velocity (in/sec)
Z = coordinate normal to flow
$\{\gamma\}$ = eigenvector (dim)
ϑ = phase angle (deg)
θ = angular displacement (rad)
μ = kinematic viscosity ($lbf\text{-}sec/in^2$)
μ_l = cell left kinematic viscosity ($lbf\text{-}sec/in^2$)
μ_r = cell right kinematic viscosity ($lbf\text{-}sec/in^2$)
$\{\phi\}$ = mass normalized eigenvector (dim)
ω = angular frequency (rad/sec)

REFERENCES

1. Boyd, J., and Raimondi, A. A., "An Analysis of Pivoted-Pad Journal Bearings," Mechanical Engineering, 75, pp 380-386, (1953).

2. Lund, J., and Peterson, L., "The Influence of Pad Flexibility on the Dynamic Coefficients of a Tilting-Pad Bearing," Journal of Tribology, 109, pp 65-70, (1987).

3. Lund, J., "Spring and Damping Coefficients for the Tilting Pad Journal Bearing," ASLE Transactions, 7, pp 342-352, (1964).

4. Nicholas, J. C., "Tilting-Pad Bearing Design," Proceedings of the Twenty-Third Annual Turbomachinery Symposium, Turbomachinery Laboratory, Texas A&M University, pp 179-194, 1994.

5. Nicholas, J. C., Gunter, E. J., and Barrett, L. E., "The Influence of Tilting-Pad Bearing Characteristics on the Stability of High Speed Rotor-Bearing Systems," Report No. UVA/643092/MAE81/141, ROMAC Laboratories, University of Virginia, (1978).

6. Armentrout, R. W., Paquette, D. J., "Rotordynamic Characteristics of Flexure-Pivot Tilting-Pad Journal Bearings," STLE Tribology Transactions, 36, pp 443-451, (1993).

7. Nicholas, J. C., Gunter, E. J., and Allaire, P. E., "Stiffness and Damping Coefficients for the Five Pad Tilting-Pad Bearing," ASLE Transactions, 22(2), pp 112-124, (1979).

8. Zadian, F. Y., "Fluid Film Bearing Fundamentals and Failure Analysis," Proceedings of the Twentieth Annual Turbomachinery Symposium, Turbomachinery Laboratory, Texas A&M University, pp 161-186, (1991)

9. Nicholas, J. C., and Wygant, K. D., "Tilting-Pad Journal Bearing Pivot Design for High Load Applications," Proceedings of the Twenty-Fourth Annual Turbomachinery Symposium, Turbomachinery Laboratory, Texas A&M University, pp 33-48, (1995).

10. Nicholas, J. C., "Fundamental Bearing Design Concepts for Fixed-Lobe and Tilting-Pad Bearings Journal Bearing," Dresser-Rand Technical Publications, pp 51-78, (1987).

11. Earles, L. L., Palazzolo, A. B., and Armentrout, R. W., "A Finite Element Approach to Pad Flexibility in Tilting-Pad Bearings; Part 1: Single Pad Analysis," ASME Journal of Tribology, 112, pp 169-176, (1990).

12. Bouard, L., Fillon, M., and Frene, J., "Comparison Between Three Turbulent Models – Application to Thermohydrodynamic Performances of Tilting-Pad Journal Bearings, Tribology International, 29, pp 11-18, (1996).

13. Armentrout, R. W., He, M., Haykin, T., and Reed, A. E., "Analysis of Turbulence and Convective Inertia in a Water-Lubricated Tilting-Pad Journal Bearing Using Conventional and CFD Approaches," STLE Tribology Transactions, 36, pp 443-451, (2016).

14. He, M., "TEHD Analysis of Fluid Film Journal Bearings", Ph. D. Thesis, University of Virginia, (2002).

15. Branagan, L. A., "Enhancements in the Thermal Analysis of Fixed and Tilting Pad Bearings Including Cross-Film Viscosity and Deformation Effects," Ph. D. Dissertation, University of Virginia, (1988).

16. Ettles C., "The Analysis and Performance of Pivoted Pad Journal Bearings Considering Thermal and Elastic Effects," Journal of Lubrication Technology, 103, pp. 182-192.

17. Armentrout, R. W., Wilson, G. J., "Reduced Shaft Stiffness Lowers Running Speed Bearing Loads and Vibration in a Single-Stage Compressor," Proceedings of the Twenty-Second Turbomachinery Symposium, Turbomachinery Laboratory, Texas A&M University, pp 33-44, (1993).

18. Childs, D. W., "Turbomachinery Rotordynamics with Case Studies - Case Study 4; Shifting an Overhung Compressor Critical Speed by Softening the Shaft", Armentrout and Wilson, pp 85-89, (2013).

19. Knight, J., and Barrett, L., "Analysis of Tilting-Pad Journal Bearings with Heat Transfer Effects", ASME paper 87-Trib-45, (1987).